High-performance anion-exchange membrane water electrolysers using NiX (X = Fe,Co,Mn) catalyst-coated membranes with redox-active Ni–O ligands

M. Klingenhof[1,9], H. Trzesniowski[2,9], S. Koch[3,4], J. Zhu[5], Z. Zeng[6], L. Metzler[3,4], A. Klinger[7], M. Elshamy[3], F. Lehmann[1], P. W. Buchheister[1], A. Weisser[8], G. Schmid[7], S. Vierrath[3], F. Dionigi[1], and P. Strasser[1]

[1]Technische Universität Berlin, Berlin, Germany.
[2]Department of Atomic-Scale Dynamics in Light-Energy Conversion, Helmholtz-Zentrum Berlin für Materialien und Energie, Berlin, Germany.
[3]Laboratory for MEMS Applications, IMTEK Department of Microsystems Engineering, University of Freiburg, Freiburg, Germany.
[4]Hahn-Schickard, Freiburg, Germany.
[5]Department of Materials Science and Engineering, National University of Singapore, Singapore, Singapore.
[6]Davidson School of Chemical Engineering, Tarpo Department of Chemistry, Purdue University, West Lafayette, IN, USA.
[7]Siemens Energy Global GmbH & Co. KG, SE TI SES PRM, Erlangen, Germany.
[8]Nanoscale Solid–Liquid Interfaces, Helmholtz-Zentrum Berlin für Materialien und Energie, Berlin, Germany.

[9]These authors contributed equally: M. Klingenhof, H. Trzesniowski.

Abstract

Recent efforts in anion-exchange membrane water electrolysis (AEMWE) focus on developing superior catalysts and membrane electrode assemblies to narrow the performance gaps compared with proton-exchange membrane water electrolysis (PEMWE). Here we present and characterize Ir-free AEMWE cells with NiX (X = Fe, Co or Mn) layered double hydroxide (LDH) catalyst-coated membranes with polarization characteristics and hydrogen productivities approaching those of acidic PEMWE cells, achieving >5 A cm^{-2} at <2.2 V. Operando spectroscopy revealed a correlation between Ni^{4+} centres and redox-active O ligands with an O K-edge feature, attributed to μ_3-O ligands in the γ-LDH catalytic phase via density functional theory calculations. This computational–experimental study challenges the previously assumed correlation between spectral O K-edge features and oxygen evolution reaction performance in Ni-based LDH catalysts and provides insights from the molecular to the technological level demonstrating how redox-active Ni–O species and innovative catalyst-coated membrane preparation boost AEMWE performance to values rivalling state-of-the-art PEMWE cell technology.

Main

Green hydrogen produced via water electrolysis powered by renewable energy is attracting much attention in the transformation process of our energy and industry systems. Today, there are three major types of low-temperature water electrolysers at varying technology maturity levels: proton-exchange membrane (PEM) water electrolysis (PEMWE), liquid alkaline water electrolysis (AWE) and anion-exchange membrane (AEM) water electrolysis (AEMWE). PEMWE is an early market energy technology for supplying green hydrogen. The main appeal of PEMWE cells and stacks arises from their high current densities >5 A cm^{-2} at cell voltages below 2 V in research cells, in part thanks to low membrane resistance. This is conducive to reduced stack sizes and low capital expenditures. Also, PEMWE is the most load-flexible of the three technologies. However, PEMWE requires the deployment of scarce noble metal catalysts, perfluorinated membranes and ionomers, and noble metal-coated stack components to sustain the highly acidic environment[1,2,3]. This may cause high and possibly unpredictable material cost and supply limitations at larger scales[4,5,6]. AWE cells allow the use of low-cost component materials, an advantage that is offset by limited current and power densities, the corrosive electrolyte coupled to reduced load flexibility. As a result, large stack sizes are required for AWE, causing long start-up and shut-down times, thus limiting integration with fluctuating renewable energy.

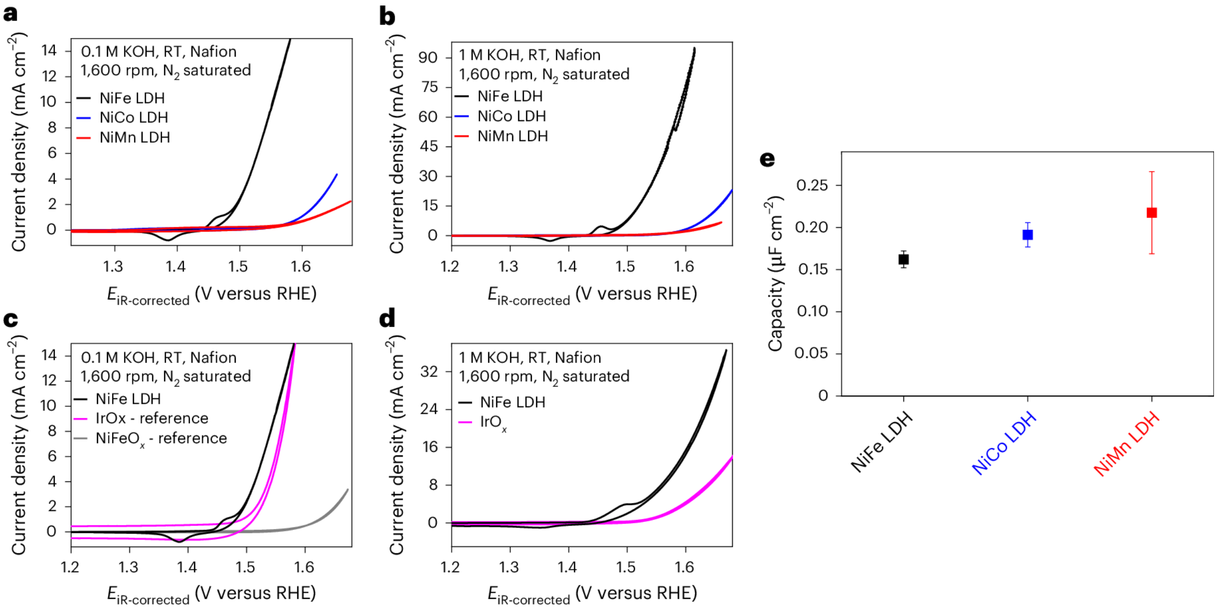

Fig. 1: OER activities of NiX LDH electrocatalysts.

a–**d**, Three-electrode rotating disk electrode measurements investigating the electrochemical properties of NiX LDH catalysts (X = Fe (black), Co (blue), Mn (red)) and commercial reference catalysts (IrO$_x$ (magenta) and NiFeO$_x$ (grey)). Comparison of linear scan voltammetry and OER activity of NiFe, NiCo and NiMn LDH in 0.1 M KOH (**a**) and 1 M KOH (**b**). **c**, The OER activity of NiFe LDH (black) compared with commercial IrO$_x$ (magenta) and commercial NiFeO$_x$ (grey) in 0.1 M KOH. **d**, The OER activity of NiFe LDH (black) and IrO$_x$ (magenta) in 1 M KOH after applying a stress protocol of 2,000 cycles with potential holds for 10 s at 1.23 V$_{RHE}$ and 1.63 V$_{RHE}$. **e**, Investigations of the capacitance of NiX LDHs (X = Fe, Co, Mn) applying galvanostatic electrochemical impedance spectroscopy. The measurements were conducted in N$_2$-saturated KOH solution at 1,600 rpm and room temperature (RT). The error bars in **e** are the standard deviation calculated from three independent measurements.

AEMWE combines advantages of both PEMWE and AWE: small stack sizes capable of fast start-up and shut-down and, thus, compatible with fluctuating renewable energy coupled with low-cost catalysts, stack hardware and fluorine-free membranes[1,2,3,7]. Thus, it constitutes a promising and reasonable option for large-scale sustainable production of hydrogen. As a consequence, research on AEMWE has increased notably and quickly over recent years[8]. So far, a broad variety of highly conductive and stable AEMs have emerged showing good performance in single cells[9,10,11]. While high current densities at the ampere cm^{-2} level have been reported using high Ir-loaded AEMWE anodes (with Ir loadings of up to 0.5 mg Ir cm^{-2}), this remains a grand challenge for Ir-free AEMWE cells, whose performances have been sharply falling short of state-of-the-art PEMWE cells[1,12,13,14,15]. This is why the design and availability of high-performance, Ir-free and stable AEMWE cells delivering >5 A cm^{-2} at cell potentials near 2 V has remained a major technological challenge. The present contribution will address and offer solutions to this challenge.

Herein, we report the design, assembly and component analysis of Ir-free AEMWE cells that approach the current–potential characteristics as well as hydrogen productivity of state-of-the-art acidic PEMWE cells. The AEMWE cells reported herein deliver a current density of >5 A cm^{-2} near 2 V uncorrected cell voltage. At a current density of 4 A cm^{-2}, the described AEMWE cells trail today's PEMWE cells by a mere 150 mV in terms of ohmic drop (iR)-corrected kinetic cell voltage. This is testament to the outstanding catalytic reactivity of the electrodes, in particular the NiFe layered double hydroxide (LDH) oxygen-evolving anode. At a cell voltage of 1.8 V, corresponding to a cell efficiency, η, of 82%, the present AEMWE cell continues to yield >2 A cm^{-2}. This exceptional performance was made possible using a previously unavailable catalyst-coated membrane (CCM) preparation method[15], incorporating an Ir-free NiFe LDH anode formulation with exceptional redox electrochemistry. What sets the molecular characteristics of the present CCM anode apart from other Ni-based materials[16,17] is the unusually high ratio of structural transformation of the semiconducting α-LDH phase into the conducting and catalytically active γ-LDH phase. A detailed spectroscopic analysis of the CCM anode revealed a previously elusive coupling of redox-active Ni^{4+} centres and their O ligands by using operando synchrotron soft X-ray O K-edge and Ni L-edge spectroscopy. Our spectroscopic experiments are supported by previously unavailable density functional theory (DFT)-based computational predictions of O K-edge spectra of all three LDH catalysts. In contrast to commonly held views derived from studies on iridium oxide, our computations relate the chemical and structural identity of the activated O ligands of the γ-LDH phase to a combination of μ_3-O species at basal planes and catalytically active μ_1-O and μ_2-O ligands at edge sites. As a result, for Ni-based LDH oxygen evolution reaction (OER) catalysts, we argue that a characteristic spectral O K-edge feature near 529 eV serves as an indicator for the presence of the catalytically active γ-LDH phase.

Results

Anode catalyst voltammetry

The anode of the AEMWE CCM consisted of a powder thin film of a solvothermally prepared NiFe LDH. The favourable iR-corrected kinetic cell voltages of the AEMWE cells, discussed further below, originated from the geometric and electronic properties of the NiFe LDH anode catalysts. To learn more about the molecular properties of the NiFe LDH material, we characterized it in comparison with NiCo LDH and NiMn LDH reference catalysts. Comparative electrochemical geometric area-normalized catalytic OER activities at comparable catalyst loadings of NiFe, NiCo and NiMn LDHs were obtained from rotating disk electrode measurements in alkaline electrolytes of varying KOH concentrations (Fig. 1a,b). NiMn LDH was evidently the least active OER catalyst, followed in order by NiCo LDH and NiFe LDH. Interestingly, the characteristic Ni redox wave, indicating the onset of hole injection into the Ni-based catalyst, followed a different trend, namely, NiCo < NiMn < NiFe LDH (Supplementary Fig. 1). Evidently, the detailed onset potential of the OER surface catalysis is not directly coupled to the emergence of higher Ni redox states. A comparison of our solvothermal layered NiFe LDH with commercial hydrous IrO_x and $NiFeO_x$ OER electrocatalysts highlights the benefits of the platinum group metal (PGM)-free NiFe LDH OER catalysts over conventional state-of-the-art anode catalysts (Fig. 1c). The electrochemical stability of the NiFe LDH during accelerated stress tests (ASTs; Supplementary Table 2 and Supplementary Figs. 2 and 4) relative to commercial hydrous IrO_x and relative to NiCo and NiMn LDH was investigated, and the results are depicted in Supplementary Figs. 3 and 4. Evidently, NiFe

LDH exhibited a favourable stability, which qualifies it as the most suitable AEMWE anode catalyst. Finally, Fig. 1d shows the cyclic voltammetry and catalytic OER reactivity of NiFe LDH and IrO_x after the AST in 1 M KOH. While both materials suffered from performance decays, NiFe LDH outperformed commercial IrO_x. This is probably due to irreversible redox processes of hydrous IrO_x in alkaline environments and the consequent formation of soluble Ir species, which result in severe material loss[18,19,20]. By contrast, reversible geometric transformations between the catalytic inactive α-NiFe LDH phase and the catalytic active γ-NiFe LDH phase lead to improved tolerance against dissolution during ASTs[21,22]. Even though the correlation of catalytic activity trends between rotating disk electrode and membrane electrode assembly (MEA) single cells has been reported to be challenging[23,24,25], our data and cell building procedures suggest that the present NiFe LDH OER catalyst can be processed into stable and active CCMs that reveal previously unachieved AEMWE cell power densities.

Anode catalyst surface area and interfacial capacitance

To learn more about the origin of the observed voltammetric reactivity trends, we first investigated the trend in the real electrochemical surface area (ECSA) of the three LDH catalysts. As reliable sorption techniques to determine the ECSA of oxidic powder materials have remained elusive, researchers traditionally resort to proxy characteristics, such as the area-normalized interfacial capacitance, C_{dl}, of the catalyst powder films. Values for C_{dl} are accessible from the slope of capacitive current–potential scan rate relations taken in non-faradaic potential windows. However, the non-conductive nature of Ni LDH catalyst films below the Ni redox waves precludes the use of voltammetry-derived C_{dl} values[26]. Instead, interfacial capacitance values, relevant and reliable as ECSA proxy values, are accessible using the experimentally accessible adsorbate capacitance (C_{a}) extracted from complex impedance measurements under catalytic OER operating potentials[21,27,28,29]. C_{a} is believed to represent the differential pseudocapacitive charge injected into the surface by surface redox processes and their reactive intermediates at a given electrode potential. Supplementary Note 3 provides the details of our C_{a} measurements using potentiostatic electrochemical impedance spectroscopy and galvanostatic electrochemical impedance spectroscopy. Both methods resulted in very similar adsorbate capacitances for each of the three Ni LDH materials (Fig. 1e), excluding the surface area to be a controlling factor in the observed OER reactivity trends. Thus, there must be other material characteristics accountable for the sharp catalytic reactivity differences in NiMn, NiCo and NiFe LDH.

Operando X-ray absorption spectroscopy

To learn more about the origin of the OER reactivity trends of the three Ni-based LDH catalysts, we tracked the chemical state dynamics of Ni and O atoms at selected constant applied electrode potentials and during voltammetric potential cycling. The formation of the catalytic active γ-LDH phase from the inactive α-LDH phase has previously been coupled to structural transformations involving interlayer anion ejection and cation injection linked to lattice contraction[22]. However, unlike for IrO_x electrocatalysts[30,31,32,33], little is known about the chemical state dynamics of metal centres and ligands during the formation of the catalytic active γ-LDH phase.

Figure 2a reports potentiostatic operando X-ray absorption spectroscopy (XAS) spectra of the O K-edge at a non-catalytic potential (+1.15 V_{RHE}), where the α-LDH phase is prevalent, and under conditions where the catalytic active γ-LDH phase is formed (+1.45 V_{RHE}). While the spectra of NiFe, NiCo and NiMn LDH recorded at +1.15 V_{RHE} were almost identical, that is, showing one distinct resonance at 531.3 eV related to lattice oxygen, the spectra recorded at +1.45 V_{RHE} differed substantially in their pre-edge region. Around 529 eV (528.7 eV, more precisely), the NiFe LDH catalysts have a much more intense spectral feature compared with NiCo and NiMn LDH. In the absence of a more detailed understanding of the chemical identity and geometric location of these O atoms, we refer to these O species henceforth as O-529eV. We further attribute the integral intensity of the 529 eV resonance to the fraction of the α-LDH phase that has transformed into the γ-LDH phase. We thereby refrain from the commonly held view that the O-529eV species represent catalytic active surface intermediates of the OER process. Intensely studied in hydrous Iridium oxides, this O K pre-edge feature has been firmly assigned to electron-deficient catalytic active O species featuring localized hole states, formally referred to as O^{1-} (refs. [30,31,32,33,34,35,36,37,38]). Likely by analogy, yet lacking computational analyses, the 529 eV spectral feature in Ni-based catalysts was associated with similar charge redistributions of reactive O intermediates[16,17,39,40]. Based on our computational analyses below, we challenge these previously held views, at least for the present layered γ-NiFe LDH OER catalyst phases.

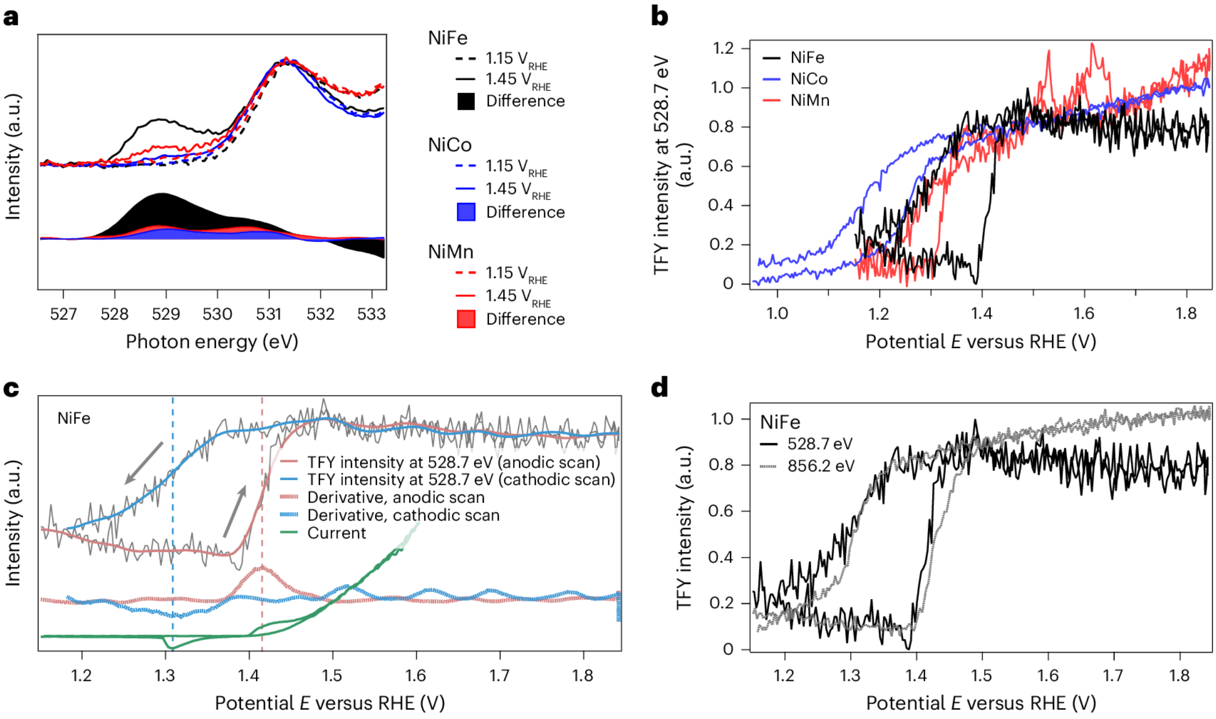

Fig. 2: Operando O K-edge XAS and following the dynamics of O-529eV.

a, Operando (pre) oxygen K-edge TFY absorption spectra of NiFe LDH (black), NiCo LDH (blue) and NiMn LDH (red) measured at 1.15 and 1.45 V versus RHE. **b**, The TFY intensity at 528.7 eV during a CV between 1.15 and 1.85 V versus RHE at 5 mV s^{-1} for NiFe LDH (black) and NiMn LDH (red) and between 0.95 and 1.85 V versus RHE for NiCo LDH (blue), respectively. **c**, A comparison of the TFY intensity at the maximum intensity of the pre-edge feature (528.7 eV) as a function of the applied potential during CV, its first derivative and the corresponding CV for NiFe LDH. **d**, A direct comparison of the TFY signal of the feature at 528.7 eV and the Ni^{4+} feature at 856.2 eV for NiFe LDH. The measurements were conducted in 0.1 M KOH at room temperature (RT).

To correlate the onset of the O-529eV species with features in the potentiodynamic surface voltammetry, we tracked the intensity of the spectral resonance at 528.7 eV during potential cycling for all three LDH catalysts as shown in Fig. 2b. We further contrasted the intensity scans individually with their own derivative and their voltammetry in Fig. 2c and Supplementary Fig. 9a,c. Figure 2b shows how each LDH catalyst exhibited its own distinct onset electrode potential of the O-529eV species associated with the formation of the γ-LDH phase, in the order NiCo (1.15 V_{RHE}) < NiMn (1.30 V_{RHE}) < NiFe (1.4 V_{RHE}). The γ-LDH phase onset potentials thereby match precisely the voltammetric metal redox waves, in both the anodic and cathodic scan direction, retracing the characteristic voltammetric metal redox hysteresis. These results confirm that the

O-529eV species form concomitantly to Ni redox states >2 and disappear accordingly. We note that the onset potentials of O-529eV species also fully match those reported from operando X-ray diffraction studies of the atomic lattice structure of Ni-based LDH catalysts[21]. We conclude that LDH lattice bulk geometry and the emergence of O-529eV species appear to be closely coupled.

To get more detailed insight into the Ni redox state(s) upon formation of O-529eV species, we tracked the XAS spectral intensity at 856.2 eV, associated with Ni^{4+} (Supplementary Fig. 10)[16], during voltammetric cycling and correlated it with the spectral O K-edge 528.7 eV resonances for NiFe LDH (Fig. 2d), NiCo LDH (Supplementary Fig. 9b) and NiMn LDH (Supplementary Fig. 9d). For all LDH catalysts, the 856.2 eV and 528.7 eV signatures track each other closely in both scan directions. This striking similarity in the potential hysteresis suggests a close coupling of the redox transition from Ni^{2+} to Ni^{3+}/Ni^{4+} and the formation of O-529eV species that indicate the formation of the γ-LDH phase. To elucidate the structural transitions of electrocatalysts, various operando characterization methods can be employed, with operando X-ray scattering being one of the prominent techniques[41,42,43,44]. For more insight into the correlation of structural and electronic information please refer to Supplementary Fig. 11 and Supplementary Note 6. Additional characterizations such as high-resolution X-ray diffraction or high-resolution transmission electron microscopy could further support the assignment of the γ-phase. While an atomic proximity between Ni^{4+} centres and O-529eV species appears conceivable, a causation between the two processes remains unclear. The direct evidence for the immediate presence of Ni^{4+} in the γ-LDH phase is an important mark of distinction compared with previously investigated $NiFeO_x$ OER catalysts, where the detection of Ni^{4+} has remained elusive. This underlines the exceptional redox activity of our wet-chemically synthesized layered NiFe LDH catalyst deployed in the AEMWE cells below.

To establish a link to the catalytic evolution of molecular O_2, we note that, for NiFe LDH, the Ni^{2+} to Ni^{4+} transition occurs between 1.40 and 1.45 V_{RHE} and starts to disappear below 1.35 V_{RHE}. The actual onset potential of molecular oxygen evolution, judged from differential electrochemical mass spectrometry[22], lies more anodic of 1.45 V_{RHE}. This is even more so for NiMn and NiCo LDH. Thus, we conclude that the Ni^{4}-O-529eV states evolve before the evolution of O_2. In other words, the presence of the γ-NiFe LDH phase is a necessary but not sufficient condition for the evolution of molecular oxygen. We suspect that additional kinetic energy barriers need to be overcome before oxygen evolution sets in. The magnitude of the kinetic barriers as well as the elementary step associated with them can thereby vary among LDH catalysts with distinct trivalent metals. In fact, a previous comparative mechanistic analysis of NiFe, NiCo and NiMn LDH revealed that the (thermodynamic) limiting potentials, that is, the electrode potentials where the last of the four elementary reaction steps becomes downhill, are 1.68 V, 1.88 V and 1.94 V, respectively. These values are more anodic than the calculated and experimentally observed α- to γ-LDH transformation potentials. Furthermore, the last elementary step to become downhill is *OH → *O for NiFe LDH, while it is *OOH → O_2 for NiCo and NiMn (ref. [21]).

Computational structural and chemical identification of O-529eV ligands

To elucidate the chemical and geometric origin and identity of the O-529eV species in γ-LDH phases, we carried out DFT predictions of absorption spectra of Ni-based LDH catalysts. The atomic structures of the catalytic inactive α-NiFe LDH model with the formula $Ni_6Fe_2(OH)_{16}\cdot CO_3\cdot 4H_2O$ are shown in Supplementary Figs. 12a and 13a and those of the γ-NiFe LDH model with the formula $Ni_6Fe_2O_{16}\cdot 2\,K\cdot 4H_2O$ in Fig. 3a and in Supplementary Figs. 12b and 13b. To account for individual variations, we calculated the O K-edge absorption spectra for oxygen atoms in the top ten layers (see numbered atoms in Fig. 3b and Supplementary Fig. 12a,b). The computational spectra for the OH in α-NiFe LDH did not show resonances near 529 eV, which agrees with our experimental results. By contrast, as anticipated from the O K-edge XAS experiments, the OER active γ-NiFe LDH phase showed notable differences from the α-NiFe LDH phase in the pre-edge region.

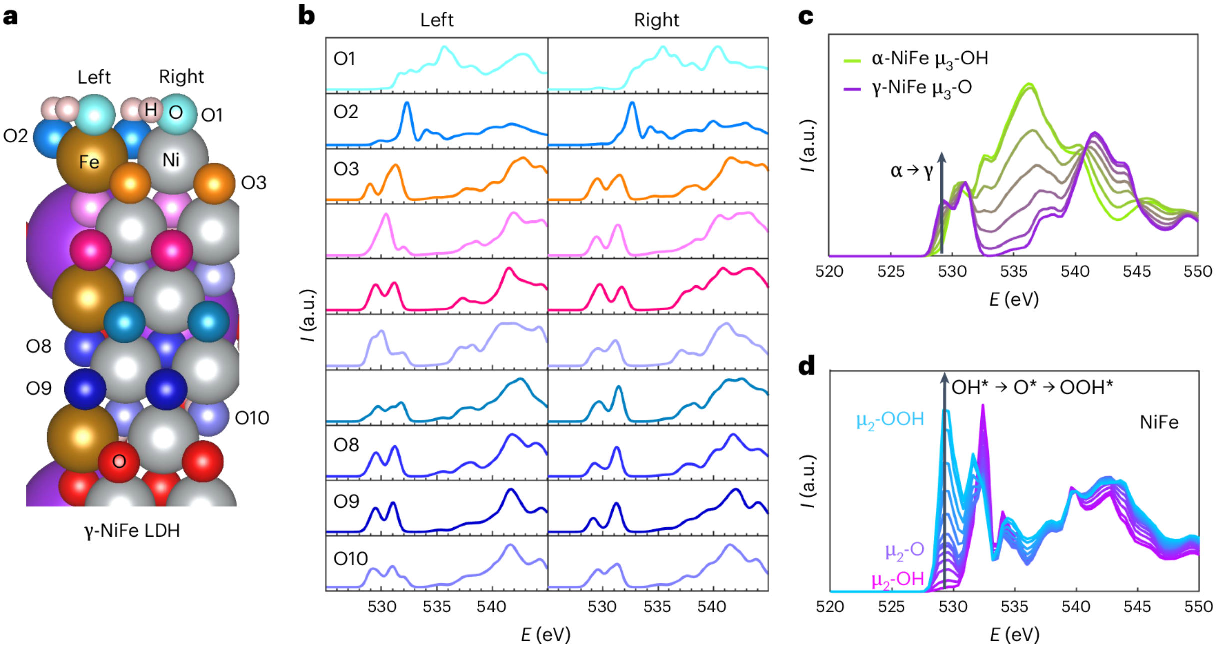

Fig. 3: Computational O K-edges.

a, The atom structure of γ-NiFe LDH. The oxygen atoms at different depths from the surface are represented by different colours. **b**, The computational O K-edge of individual oxygen atoms at the top ten layers with two atoms at each layer. The curve colours are consistent with the atom colours in **a**. All curves are normalized by the maximal values in the whole range. **c**, The average O K-edge of all oxygen atoms at the hollow sites of α- and γ-phases, and the combination of various α/(α+γ) ratios of 0.1, 0.3, 0.5, 0.7 and 0.9, respectively. All curves are normalized by the maximal values in the energy range around 531 eV. **d**, The computational O K-edge of an individual oxygen atom at the bridge site in different OER intermediate OH*, O* and OOH*, and the combination of various OH*/(OH*+O*) and O*/(O*+OOH*) ratios of 0.1, 0.3, 0.5, 0.7 and 0.9, respectively. All curves are normalized by the maximal values near the main peak (around 540 eV; among this range, all curves are almost identical).

While the spectra of surface OH (both one-coordinated atop μ_1-OH and two-coordinated bridge μ_2-OH) do not show notable features at 529 eV, the oxygen atoms in the subsequent eight layers (O3–O10) demonstrate pronounced absorption features at that energy. These oxygen atoms are associated with three-coordinated terrace sites (μ_3-O), which are present in the brucite-like planes of the OER active γ-NiFe LDH phase. Consequently, the oxygen ligands probably responsible for the 529 eV resonance appear to be the μ_3-O motifs.

Figure 3c illustrates the spectral changes in the O K-edge during the transformation from α- to γ-NiFe LDH by presenting different ratios of the average spectra of individual oxygen atoms in the α- and γ-NiFe LDH phase (the respective computational spectra of NiCo and NiMn LDH are given in Supplementary Figs. 13, 16 and 17). The hybridization between the 3*d* orbital of the transition metal and the oxygen 2*p* orbital increased as the bond length shortened, and coordination remained unchanged during the oxidation process of octahedral Ni^{2+} and Fe^{3+} in α-NiFe LDH to Ni^{3+}/Ni^{4+} and Fe^{4+} in γ-NiFe LDH. It is apparent that the signal at 529 eV increased with increasing fraction of the γ-phase. Hence, the protonated μ_3 species in the bulk of the α-phase do not have a resonance at 529 eV, while the deprotonated μ_3 species in the γ-phase do show a signal near 529 eV. These computational observations confirmed that the spectral resonance near 529 eV in

LDH materials can be related to the transformation from α- to γ-NiFe LDH, representing the shift from the inactive to the catalytic active phase.

To track the spectral changes during OER, we simulated O K-edge spectra of various reaction intermediates situated at the bridge site of γ-NiFe (01–10) surface, as shown in Fig. 3d. During the OER process, when bridge-OH is oxidized to O, the intensity of the peak at 529 eV increased. This indicates a stronger covalent bonding between the metal and oxygen. Similarly, in the subsequent step when O* is attacked by OH^- to form OOH*, the intensity of the peak at 529 eV increased, as well. Thus, if either OOH formation or O_2 desorption is the rate-determining step, surface intermediates O* or OOH* would contribute to the peak at 529 eV in the O K-edge spectra.

While the relative intensity of peaks at 529 eV with respect to the main peaks in Fig. 3d varies for different intermediates (μ_2-OH/O/OOH), distinguishing them in experimental XAS spectra remains a challenging task. To contextualize these findings with the previously discussed experimental XAS spectra from Fig. 2, we propose that the main contribution of the spectral features near 529 eV derives from μ_3-O species located in the bulk of γ-NiFe LDH. On the other hand, μ_2-O and μ_2-OOH, which are present at the catalyst edge surface, also contribute to the 529 eV peak, but to a minor extent owing to the larger abundance of bulk μ_3-O species, compared with edge and defect μ_2-O and μ_2-OOH species. These results demonstrate that it is challenging to assign a numerical valence state to the oxygen species responsible for the resonance near 529 eV in catalytic active NiFe oxides. Contributions of distinct species are convoluted. In this context, we recall that, while for OER active iridium oxides the spectral resonance near 529 eV has repeatedly associated with electrophilic O^{I-} species[30,31,32,33,34,35], this assignment is purely formal in character and unlikely to reflect the physical reality. Finally, comparative calculations of surface OH*-saturated and surface O^--covered NiFe LDH surfaces (Supplementary Figs. 14 and 15 and Supplementary Note 6) showed that electrophilic (electron-deficient) $O^{(II-\delta)-}$ oxygen species indeed contribute to the peak at 529 eV in the O K-edge of NiFe LDH. However, this contribution is notable only at potentials above 2 V (Supplementary Figs. 16–19 and Supplementary Notes 7 and 8). We conclude from our computational investigations of NiX (X = Fe, Mn or Co) LDH catalysts that the 529 eV feature in the O K-edge is associated with the activation of the NiX LDH catalyst phase to the OER active and conductive γ-phase.

Preparation of NiFe LDH-coated alkaline exchange membranes

Our insight into the favourable extent of phase transformation of the α-LDH into the γ-LDH phase proved a practical selection criterion of a suitable anode electrocatalyst for deployment as a catalyst layer in technological MEAs. Catalyst layers with catalyst loadings of about 1 mg cm^{-2} represent a key component of CCMs of AEMWE cells. Since inactive α-NiFe LDH will not contribute to the electrolyser performance owing to the absence of catalytic active O ligands, promising catalyst candidates should show a high conversion to the γ-phase. The NiFe LDH catalyst presented in this work showed an exceptionally high redox activity of the Ni–O ligand and, thus, was chosen as the anode catalyst material for the preparation of CCM for subsequent AEMWE single-cell testing.

While PEMWE technology relies on a hot pressing decal transfer of thick anode catalyst layers onto cation exchange membranes, the high glass transition temperature of AEMs prevents the use of this coating technique in the area of AEMWE. In addition, since direct catalyst coating onto AEMs has been challenged by membrane swelling and shrinking, which result in unstable catalyst layers, today's AEMWE cell assembly largely relies on catalyst-coated substrate procedures[15]. We report the preparation of directly catalyst-coated AEMs using a wet-film bar-coating technique. After direct application of the catalyst ink to the membrane, the coating was stabilized and protected using a combination of a polytetrafluoroethylene (PTFE) inner foil and an adhesive outer foil. The adhesive foil allowed fixation of the half CCM for direct coating of the counter electrode (CE). Details are provided in Supplementary Information. This coating procedure enabled the previously elusive generation of stable and uniform powder catalyst layers on swelling AEMs. Catalyst loadings were controlled by a choice of the catalyst layer thickness.

AEMWE single-cell measurements using NiFe LDH CCMs

AEMWE cell measurements were conducted using CCM-based MEA incorporating the NiFe LDH anode. The electrochemical hydrogen productivity (cell polarization curve), probed in terms of the measured cell potential as function of the applied current density, and the AEMWE cell stability, probed as variations in cell potential at a constant current density, were assessed in a two-electrode zero-gap configuration at 60 °C and 80 °C (Supplementary Fig. 20). Figure 4a shows much higher current densities at 80 °C compared with 60 °C. At 60 °C, a current of 2 A cm^{-2} was achieved at 1.9 V, while at 80 °C, 2 A cm^{-2} was achieved below 1.8 V. A current density of 2.3 A cm^{-2} was obtained at a cell voltage of 1.8 V. Unlike reported AEMWE cell designs that experienced severe mass transport losses below 5 A cm^{-2}, our AEMWE cell design remained kinetically and ohmic loss controlled up to current densities above 5 A cm^{-2}. A current density of 5.5 A cm^{-2} was reached at around 2.2 V cell voltage. These polarization values were not dictated by limitations of the AEMWE cell but were related to hardware limitations of the current booster.

Importantly, when compared with a state-of-the-art PEMWE polarization curve (magenta in Fig. 4)[45], the AEMWE cell design presented here featured comparable current densities but at fully Ir-free electrodes[45]. The iR-corrected polarization curves (Fig. 4a) display a mere 150 mV kinetic voltage difference at 4 A cm^{-2}. This modest performance gap holds immense advantages considering the cost impact associated with Ir-loaded anodes.

The present AEMWE cells also exhibited decent performance stability for over 110 h at a constant electrochemical load of 1 A cm^{-2}. At 60 °C and 80 °C, the observed cell potential increase amounted to 600 μV and 613 μV per hour, respectively (Fig. 4c). The majority of potential increase occurred within the initial operating hours. Consequently, at this point, a current density of 1 A cm^{-2} can be safely sustained for at least 110 h of operation below a cell voltage of 1.8 V.

Conclusions

We have demonstrated Ir-free AEMWE cells with previously unavailable polarization characteristics and hydrogen productivities that closely approach those of today's state-of-the-art acidic PEMWE cells. The AEMWE cells delivered a current density of >5 A cm^{-2} near 2 V uncorrected cell voltage. At a current density of 4 A cm^{-2}, the AEMWE cells lagged behind reported PEMWE cells by a mere 150 mV (ref. [45]). The AEMWE cell design with alkaline CCMs was made possible by a scalable bar-coating process involving the use of an adhesive foil to minimize membrane swelling during the coating of the second catalyst layer[15].

Beyond CCM process innovations, we attribute the cell performance to the molecular characteristics of NiFe LDH catalysts, which were benchmarked against NiMn LDH and NiCo LDH catalysts. In a combined experimental and DFT-computational effort to understand the high catalytic reactivity of the NiFe LDH anode, we reached deeper chemical and structural insights of relevant redox-active oxygen ligands.

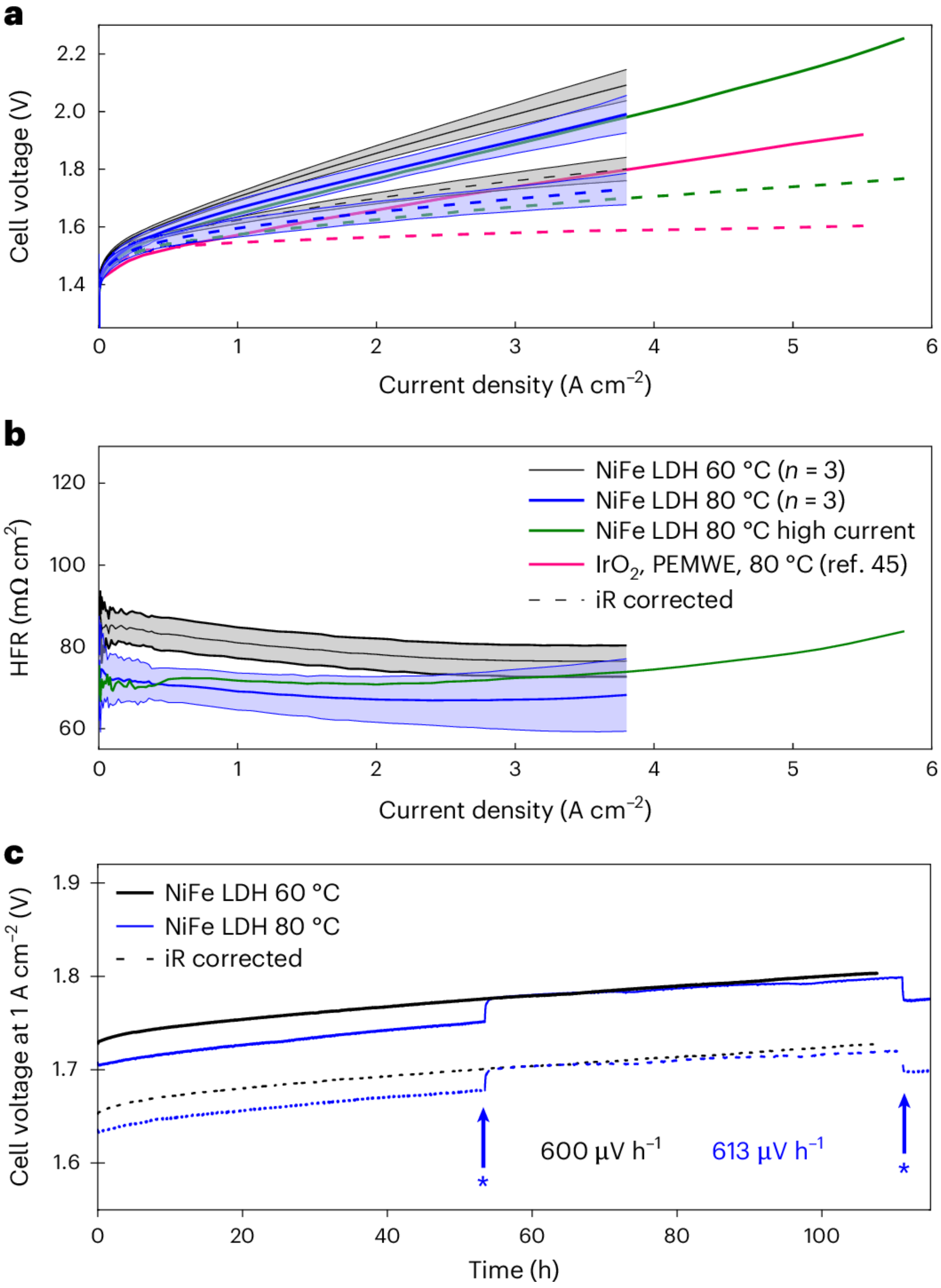

Fig. 4: AEMWE single-cell measurements using NiFe LDH CCMs.

a, Polarization curve measurements of CCM-based AEMWE single cells with 1.0±0.2 mg NiFe-LDH cm^{-2} and 0.5±0.1 mg Pt cm^{-2} in 1 M KOH. AEMWE single-cell measurements at 60 °C (black) and 80 °C (blue) and up to 5.5 A cm^{-2} (olive) in comparison with state-of-art PEMWE polarization (magenta). Shaded areas show 95% confidence intervals (*n* = 3; individual cells). Dashed lines denote high frequency resistance (HFR) corrected curves. **b**, HFR values plotted against the current density of the measurements shown in **a**. **c**, Constant current cell operation at 1.0 A cm^{-2} of the AEMWE cells at 60 °C (black) and 80 °C (blue) over 110 h. Dotted lines denote HRF corrected data. The asterisk at 53 h marks the time point where the cell's temperature was altered to 70 °C. The asterisk at 110 h indicates the increase to 80 °C again.

Contrary to commonly held views, the spectroscopically probed oxygen species associated with the XAS O K spectral feature near 529 eV under OER relevant potentials were largely μ_3-O ligands in the bulk, rather than catalytically active μ_2-O ligands on the surface. Hence, this spectral feature largely indicates the extent of the formation of the catalytically active γ-LDH phase, rather than being a direct measure of coverage of catalytic active intermediates for the release of molecular oxygen, as reported in previous spectroscopic studies of IrO_x OER catalysts. We further uncovered the unexpected presence of Ni^{4+} at non-catalytic electrode potentials for all three examined LDH catalysts. The potential dependence of this feature correlates with the one at 529 eV, suggesting a strong coupling between the two and the formation of the catalytically active γ-LDH phase.

Our findings imply that actual oxygen evolution is not solely reliant on the appearance of the absorption feature at 529 eV and the presence of Ni^{4+}, suggesting that additional kinetic barriers play a substantial role.

Taken together, this contribution demonstrates that advanced Ir-free and F-free AEMWE cells are rivalling established state-of-the-art PEMWE cell technology, providing a promising path towards more cost-effective and scalable hydrogen production solutions. Moreover, the herein presented work highlights the correlation between electronic and structural characteristics in electrocatalysts, which can only be unravelled by combining operando experiments with theoretical calculations. Understanding of such correlations is crucial for advancing the development of efficient catalysts for water electrolysis.

Methods

Synthesis of the applied NiX-LDH materials

NiFe LDH was synthesized in a solvothermal one-pot synthesis route using a microwave-assisted autoclave (Anton-Paar 300 Monowave) as described by Klingenhof et al.[46]. Prepared aqueous precursor solutions consisting of 1,200 µl of 0.6 M $Ni(OAc)_2{\cdot}4\,H_2O$ (Sigma-Aldrich, 99.998% purity) and 180 µl of 0.6 M $Fe(NO_3)_3{\cdot}9\ H_2O$ (Alfa Aesar, 98% purity) were added to 6 ml of dimethylformamide (Sigma-Aldrich) and subsequently stirred for 12 h. Subsequently, 8 ml of ultrapure water (>18 MΩ at room temperature) and 4 ml of additional dimethylformamide were added to the reaction mixture. The solution was then microwave-treated at 120 °C for 60 min followed by 30 min at 160 °C. The final product was collected by centrifugation, then repetitively washed with ethanol and ultrapure water and finally freeze-dried. In the case of NiCo LDH and NiMn LDH, 0.6 M solutions of cobalt(II) acetate tetrahydrate (Alfa Aesar, 98.0%) and manganese(II) acetate tetrahydrate (Sigma-Aldrich, >99.0%) were used instead of 0.6 M $Fe(NO_3)_3{\cdot}9\ H_2O$.

Electrochemical evaluation of the catalyst activity and stability

For electrocatalytic activity testing, a catalyst suspension was prepared. The suspension consists of 4 mg catalyst, 768 µl *i*-PrOH, 200 µl deionized (DI) water and 32 µl 5 wt.% Nafion perfluorinated resin solution (Sigma-Aldrich). Ten microlitres of the resulting catalyst dispersion was pipetted on the GC electrode (0.1963 cm^2) to reach an overall loading of 200 $\mu g\ cm^{-2}$. The loadings were adjusted. The electrocatalytic performance of the catalyst was evaluated in N_2-saturated 0.1 M and 1 M KOH at 1,600 rpm using a Biologic SP-200 potentiostat operating in a three-electrode setup with a platinum CE and a reversible hydrogen electrode (RHE) reference electrode. All reported cyclic voltammograms (CVs) are iR corrected. The overpotentials reported, necessary to reach a current density of 10 mA cm^{-2} (OER), are the average of three measurements. To test the stability of different types of ionomer during electrochemical strain, 2,000 CVs in a certain potential range were recorded (1.23 V versus RHE and 1.63 V versus RHE). The overall time of stability cycling is 16 h. The detailed electrochemical protocols are given in the following tables, which summarize the activity (Supplementary Table 1) and stability (Supplementary Table 2) protocols, respectively. Supplementary Fig. 2 depicts the stability protocol based on the cyclic voltammetry advanced (CVA) technique from the Biologic Software.

Operando XAS

Operando O K-edge XAS and Ni L-edge XAS were performed in total fluorescence yield (TFY) mode with the LiXEdrom setup at the soft X-ray beamline U49-2_PGM-1 at the synchrotron-radiation facility BESSY II, Berlin, Germany. Solutions of the respective LDH and Nafion in *i*-PrOH and water (4 mg catalyst, 768 µl *i*-PrOH, 200 µl DI water and 32 µl Nafion (5 wt.% solution in alcohol)) were dropcasted onto Au-coated SiN_x membranes. The LDH ink was applied onto the SiN_x membranes in ten steps of 5 µl with a minimum of 10 min of drying between each drop. The CCM was inserted into an electrochemical flow cell designed by Tesch et al.[47], which was used for the electrochemical activation and for recording of operando TFY-XAS spectra. A scheme of the setup is displayed in Supplementary Fig. 8. The electrolyte, 0.1 M Fe-free KOH (previously purified following the procedure described by Trotochaud et al.[26], starting electrolyte: 30 wt.% NaOH in water, Suprapur), was pumped through the cell via a syringe pump at a rate of 50 µl min^{-1}. A leak-free Ag/AgCl electrode (Innovative Instruments LF-1.6, 3.4 M AgCl) was used as the reference electrode and a Pt wire as CE. The Au layer on top of the SiN_x membranes served as the connection for the working electrode. Potentials were applied with a BioLogic potentiostat (SP-200, BioLogic Scientific Instruments). Before operando XAS measurements, the samples were treated by cycling 50 times between 1.15 and 1.85 V versus RHE at 50 mV s^{-1}. All spectra were normalized to the incoming photon flux.

Computational methods

Self-consistent, periodic DFT calculations were performed with the projector augmented wave method[48,49], as implemented in the Vienna Ab-initio Simulation Package[50]. To achieve a highly accurate description of strongly-correlated LDHs with weak interaction between layers, we employ an error alignment and error cancellation approach that was developed in our recent work[51]. More specifically, this approach includes use of a Hubbard *U* term[52] to correct for self-interaction errors in 3*d* transition metal cations, a van der Waals functional optPBE[53] to describe the weak interaction that occurs between layered materials, and intercalated water and ions between layers, and use of a water-based reference state for the calculations to avoid incorrect description of the gas phase O_2 reference with standard DFT generalized gradient approximation methods. Its accuracy is demonstrated through redox and (de)hydration of Mn, Fe, Co and Ni based bulk oxides and (oxy)hydroxides with standard errors of 0.04 eV per reaction formula unit. Its performance on surface thermodynamics is also demonstrated in our recent work[21,22]. *U* values, which are applied to *d* orbitals of Fe, Co and Ni, are taken as 2.5 eV, 3.5 and 5.2 eV, respectively. A cut-off energy of 400 eV is employed. Monkhorst–Pack *k*-point grids (4 × 3 × 1) are used for Brillouin zone integration. The equilibrium geometries are obtained when the maximum atomic forces are smaller than 0.01 eV $Å^{-1}$ and when a total energy convergence of 10^{-5} eV is achieved for the electronic self-consistent field loop.

AEMWE measurements

Initial measurements of AEM (AP2-HNN8-X-50, lot 2117L04) and anion-exchange ionomer (Aemion$^+$ AP2-HNN6-00-X, lot JMY191201 and AP2-HNN8-00-X, lot JMY200701) were carried out with AP2-HNN6 as a binder. Later measurements were carried out with AP2-HNN8 as a binder

(Supplementary Table 6). The change had no influence on the performance. Polarization curves in Fig. 4 are the result of three measurements each, where one of each temperature is made with HNN6. There was no specific reason for this; it was rather a consequence of material availability and simultaneous developments in various MEA components. AEM and anion-exchange ionomer were provided by Ionomr Innovations. NiFe LDH (this work) and Pt/C (50 wt.%, Umicore, Elyst Pt50 0550–3000110038) were used as catalysts. MeOH (≥99.9%) was purchased from Carl Roth. Potassium hydroxide (KOH) pellets (85%, VWR) were used to prepare KOH solutions. Nickel fibre felts (0.2 mm) were purchased from Bekaert, and Freudenberg H24C5 carbon paper with a microporous layer was purchased from The Fuel Cell Store. PTFE sheets were purchased from Böhme-Kunststofftechnik as gasket, spacer and casting substrate materials. ZrO_2 grinding balls (Retsch, 5 mm, 22.455.0009) were used for ink mixing.

MEAs with an active area of 5 cm^2 comprised a CCM, nickel felts as an anode porous transport layer (PTL), carbon paper with a microporous layer as a cathode PTL and two PTFE gaskets encompassing both PTLs. The setup is presented in detail in Supplementary Fig. 20.

Cathode inks consisting of Pt/C 50 (0.3 g), DI H_2O (1.8 g) and Aemion$^+$ solution (2.5 wt.%, 1.8 g) were combined in a 20 ml glass vial. After adding ZrO_2 grinding balls, the vials were left on a roller mixer (IKA, ROLLER 10 digital, 0004013000) for 2 days at 80 rpm. For the anode ink, NiFe LDH (0.3 g) was treated with water (0.9 g), a mixture of MeOH:H_2O (10:1, 0.45 g) and Aemion$^+$ solution (5 wt.%, 0.45 g) in MeOH:H_2O (10:1) in a 10 ml glass vial. After adding ZrO_2 grinding balls, the vials were left on a roller mixer for 2 days at 80 rpm. In the case of NiFe LDH inks, variations in viscosity were observed. Undesirable high viscosities were counteracted by the addition of small amounts of MeOH/H_2O (for example, 150 µl) followed by a brief vigorous mixing using a vortex device (Scientific Industries, Vortex Genie 2). CCMs were fabricated by directly depositing the inks on the membrane (monolythic 50 µm) via bar coating from both sides. After removing the back foil of the anode half CCM, the addition of an adhesive foil helped to minimize membrane swelling during the coating of the cathode catalyst layer as described by Koch and Metzler in 2022[15]. The CCM is ion-exchanged and then sandwiched between the PTFE gaskets and the PTLs; the MEA is compressed between two Au-coated Ti-flow fields with parallel flow direction, before being assembled between two polyetheretherketone plates using alignment rods to avoid moving of the components during fixture tightening.

All CCMs underwent ion exchange into the hydroxide form via soaking in 3 M KOH for 24 h followed by another 24 h in 1 M KOH solution. A potentiostat with 20 A current range (VSP300, BioLogic) was used to pre-condition the CCMs, record polarization curves and measure their degradation rates. The measurement protocol is based on the one described in Koch et al.[10]. Minor adjustments were made to the measurement protocol as follows. Cells were measured with 5 A cm^{-2} and at 1 M KOH electrolyte concentration. During the pre-conditioning of the cells, the applied voltages were reduced to 1 V, 1.4 V, 1.6 V and 1.8 V to avoid surpassing the 20 A current range limit of the potentiostat at higher voltages. After polarization curves and electrochemical impedance spectroscopy measurements, the testing protocol was terminated or continued with mid-term degradation experiments. During these mid-term tests, the cell potential was recorded at a current of 1 A cm^{-2} for up to 110 h.

Acknowledgements

Financial support by the federal ministry for education and research (Bundesministerium für Bildung und Forschung, BMBF) under grant numbers 03SF0613D 'AEMready' (P.S.), 03HY130B

‘AEM-Direkt’ (P.S.), 03SF0611E ‘H2Meer’ (P.S.) and 03SF0630C ‘ZnH2’ (P.S.) and the Project ‘ANEMEL’ (Project 101071111) (P.S.) funded by the EISMEA (European Innovation Council and SMES Executive Agency) are gratefully acknowledged. Furthermore, H.T. acknowledges support from the German Federal Ministry of Education and Research in the framework of the project Catlab (grant 03EW0015A/B). We thank S. K. Kilian for support and assistance for the single-cell measurements. We acknowledge the Helmholtz-Zentrum Berlin (HZB) for providing access to the beamline U49-2_PGM-1 at the synchrotron-radiation facility BESSY II, Berlin, Germany. We express our sincere gratitude to R. Golnak and J. Xiao for their invaluable support and assistance during the beamtime.

References

1. Khataee, A., Shirole, A., Jannasch, P., Krüger, A. & Cornell, A. Anion exchange membrane water electrolysis using Aemion™ membranes and nickel electrodes. *J. Mater. Chem. A* **10**, 16061–16070 (2022).
2. Henkensmeier, D. et al. Overview: state-of-the art commercial membranes for anion exchange membrane water electrolysis. *J. Electrochem. Energy Convers. Storage* **18**, 024001 (2021).
3. Falcao, D. S. Green hydrogen production by anion exchange membrane water electrolysis: status and future perspectives. *Energies* **16**, 943 (2023).
4. Minke, C., Suermann, M., Bensmann, B. & Hanke-Rauschenbach, R. Is iridium demand a potential bottleneck in the realization of large-scale PEM water electrolysis? *Int. J. Hydrog. Energy* **46**, 23581–23590 (2021).
5. Setzler, B. P., Zhuang, Z., Wittkopf, J. A. & Yan, Y. Activity targets for nanostructured platinum-group-metal-free catalysts in hydroxide exchange membrane fuel cells. *Nat. Nanotechnol.* **11**, 1020–1025 (2016).
6. Kiemel, S. et al. Critical materials for water electrolysers at the example of the energy transition in Germany. *Int. J. Energy Res.* **45**, 9914–9935 (2021).
7. Vincent, I. & Bessarabov, D. Low cost hydrogen production by anion exchange membrane electrolysis: a review. *Renew. Sustain. Energy Rev.* **81**, 1690–1704 (2018).
8. Du, N. et al. Anion-exchange membrane water electrolyzers. *Chem. Rev.* **122**, 11830–11895 (2022).
9. Fortin, P. et al. High-performance alkaline water electrolysis using Aemion™ anion exchange membranes. *J. Power Sources* **451**, 227814 (2020).
10. Koch, S. et al. The effect of ionomer content in catalyst layers in anion-exchange membrane water electrolyzers prepared with reinforced membranes (Aemion+™). *J. Mater. Chem. A* **9**, 15744–15754 (2021).
11. Motealleh, B. et al. Next-generation anion exchange membrane water electrolyzers operating for commercially relevant lifetimes. *Int. J. Hydrog. Energy* **46**, 3379–3386 (2021).
12. Moreno-González, M. et al. One year operation of an anion exchange membrane water electrolyzer utilizing Aemion+® membrane: minimal degradation, low H_2 crossover and high efficiency. *J. Power Sources Adv.* **19**, 100109 (2023).
13. Chen, N. et al. High-performance anion exchange membrane water electrolyzers with a current density of 7.68 A cm^{-2} and a durability of 1000 hours. *Energy Environ. Sci.* **14**, 6338–6348 (2021).
14. Park, D. H. et al. Development of Ni–Ir oxide composites as oxygen catalysts for an anion-exchange membrane water electrolyzer. *Adv. Mater. Interfaces* **9**, 2102063 (2022).

15. Koch, S. et al. Toward scalable production: catalyst-coated membranes (CCMs) for anion-exchange membrane water electrolysis via direct bar coating. *Adv. Sustain. Syst.* **7**, 2200332 (2022).
16. Wartner, G. et al. Insights into the electronic structure of Fe–Ni thin-film catalysts during the oxygen evolution reaction using operando resonant photoelectron spectroscopy. *J. Mater. Chem. A* **11**, 8066–8080 (2023).
17. Drevon, D. et al. Uncovering the role of oxygen in Ni–Fe(O_xH_y) electrocatalysts using in situ soft X-ray absorption spectroscopy during the oxygen evolution reaction. *Sci. Rep.* **9**, 1532 (2019).
18. Lee, Y., Suntivich, J., May, K. J., Perry, E. E. & Shao-Horn, Y. Synthesis and activities of rutile IrO_2 and RuO_2 nanoparticles for oxygen evolution in acid and alkaline solutions. *J. Phys. Chem. Lett.* **3**, 399–404 (2012).
19. Burke, L. D. & O'Meara, T. O. Oxygen electrode reaction. Part 2.—Behaviour at ruthenium black electrodes. *J. Chem. Soc. Faraday Trans. 1* **68**, 839–848 (1971).
20. Qi, J. et al. Understanding the stabilization effect of the hydrous IrO_x layer formed on the iridium oxide surface during the oxygen evolution reaction in acid. *Inorg. Chem. Front.* **10**, 776–786 (2023).
21. Dionigi, F. et al. Intrinsic electrocatalytic activity for oxygen evolution of crystalline 3*d*-transition metal layered double hydroxides. *Angew. Chem. Int. Ed.* **60**, 14446–14457 (2021).
22. Dionigi, F. et al. In-situ structure and catalytic mechanism of NiFe and CoFe layered double hydroxides during oxygen evolution. *Nat. Commun.* **11**, 2522 (2020).
23. El-Sayed, H. A., Weiß, A., Olbrich, L. F., Putro, G. P. & Gasteiger, H. A. OER catalyst stability investigation using RDE technique: a stability measure or an artifact? *J. Electrochem. Soc.* **166**, F458–F464 (2019).
24. Fathi Tovini, M., Hartig-Weiß, A., Gasteiger, H. A. & El-Sayed, H. A. The discrepancy in oxygen evolution reaction catalyst lifetime explained: RDE vs MEA-dynamicity within the catalyst layer matters. *J. Electrochem. Soc.* **168**, 014512 (2021).
25. Hartig-Weiss, A., Tovini, M. F., Gasteiger, H. A. & El-Sayed, H. A. OER catalyst durability tests using the rotating disk electrode technique: the reason why this leads to erroneous conclusions. *ACS Appl. Energy Mater.* **3**, 10323–10327 (2020).
26. Trotochaud, L., Young, S. L., Ranney, J. K. & Boettcher, S. W. Nickel–iron oxyhydroxide oxygen-evolution electrocatalysts: the role of intentional and incidental iron incorporation. *J. Am. Chem. Soc.* **136**, 6744–6753 (2014).
27. Jeon, S. S. et al. Active surface area and intrinsic catalytic oxygen evolution reactivity of NiFe LDH at reactive electrode potentials using capacitances. *ACS Catal.* **13**, 1186–1196 (2023).
28. Watzele, S. et al. Determination of electroactive surface area of Ni-, Co-, Fe-, and Ir-based oxide electrocatalysts. *ACS Catal.* **9**, 9222–9230 (2019).
29. Watzele, S. & Bandarenka, A. S. Quick determination of electroactive surface area of some oxide electrode materials. *Electroanalysis* **28**, 2394–2399 (2016).
30. Pfeifer, V. et al. In situ observation of reactive oxygen species forming on oxygen-evolving iridium surfaces. *Chem. Sci.* **8**, 2143–2149 (2017).
31. Nong, H. N. et al. The role of surface hydroxylation, lattice vacancies and bond covalency in the electrochemical oxidation of water (OER) on Ni-depleted iridium oxide catalysts. *Z. Phys. Chem.* **234**, 787–812 (2020).
32. Nong, H. N. et al. Key role of chemistry versus bias in electrocatalytic oxygen evolution. *Nature* **587**, 408–413 (2020).

33. Frevel, L. J. et al. In situ X-ray spectroscopy of the electrochemical development of iridium nanoparticles in confined electrolyte. *J. Phys. Chem. C* **123**, 9146–9152 (2019).
34. Pfeifer, V. et al. Reactive oxygen species in iridium-based OER catalysts. *Chem. Sci.* **7**, 6791–6795 (2016).
35. Pfeifer, V. et al. The electronic structure of iridium oxide electrodes active in water splitting. *Phys. Chem. Chem. Phys.* **18**, 2292–2296 (2016).
36. Massue, C. et al. Reactive electrophilic O^{I-} species evidenced in high-performance iridium oxohydroxide water oxidation electrocatalysts. *ChemSusChem* **10**, 4786–4798 (2017).
37. Nong, H. N. et al. A unique oxygen ligand environment facilitates water oxidation in hole-doped $IrNiO_x$ core–shell electrocatalysts. *Nat. Catal.* **1**, 841–851 (2018).
38. Reier, T. et al. Molecular insight in structure and activity of highly efficient, low-Ir Ir–Ni oxide catalysts for electrochemical water splitting (OER). *J. Am. Chem. Soc.* **137**, 13031–13040 (2015).
39. Suntivich, J. et al. Estimating hybridization of transition metal and oxygen states in perovskites from O K-edge X-ray absorption spectroscopy. *J. Phys. Chem. C* **118**, 1856–1863 (2014).
40. Lafuerza, S. et al. Origin of the pre-peak features in the oxygen K-edge X-ray absorption spectra of $LaFeO_3$ and $LaMnO_3$ studied by Ga substitution of the transition metal ion. *J. Phys. Condens. Matter* **23**, 325601 (2011).
41. Magnussen, O. M. et al. In situ and operando X-ray scattering methods in electrochemistry and electrocatalysis. *Chem. Rev.* **124**, 629–721 (2024).
42. Chatenet, M. et al. Water electrolysis: from textbook knowledge to the latest scientific strategies and industrial developments. *Chem. Soc. Rev.* **51**, 4583–4762 (2022).
43. Ding, H., Liu, H., Chu, W., Wu, C. & Xie, Y. Structural transformation of heterogeneous materials for electrocatalytic oxygen evolution reaction. *Chem. Rev.* **121**, 13174–13212 (2021).
44. van Oversteeg, C. H. M., Doan, H. Q., de Groot, F. M. F. & Cuk, T. In situ X-ray absorption spectroscopy of transition metal based water oxidation catalysts. *Chem. Soc. Rev.* **46**, 102–125 (2017).
45. Bernt, M., Siebel, A. & Gasteiger, H. A. Analysis of voltage losses in PEM water electrolyzers with low platinum group metal loadings. *J. Electrochem. Soc.* **165**, F305–F314 (2018).
46. Klingenhof, M. et al. Modular design of highly active unitized reversible fuel cell electrocatalysts. *ACS Energy Lett.* **6**, 177–183 (2020).
47. Tesch, M. F. et al. Vacuum compatible flow-cell for high-quality in situ and operando soft X-ray photon-in-photon-out spectroelectrochemical studies of energy materials. *Electrochem. Sci. Adv.* **2**, e2100141 (2021).
48. Blöchl, P. E. Projector augmented-wave method. *Phys. Rev. B* **50**, 17953–17979 (1994).
49. Kresse, G. J. D. et al. From ultrasoft pseudopotentials to the projector augmented-wave method. *Phys. Rev. B* **59**, 1758–1775 (1999).
50. Kresse, G. F. Efficient iterative schemes for ab initio total-energy calculations using a plane-wave basis set. *Phys. Rev. B* **54**, 11169–11186 (1996).
51. Zeng, Z. et al. Towards first principles-based prediction of highly accurate electrochemical Pourbaix diagrams. *J. Phys. Chem. C* **119**, 18177–18187 (2015).
52. Dudarev, S., Botton, G., Savrasov, S., Humphreys, C. & Sutton, A. Electron-energy-loss spectra and the structural stability of nickel oxide: an LSDA.U study. *Phys. Rev. B* **57**, 1505–1509 (1998).
53. Klimes, J., Bowler, D. R. & Michaelides, A. Van der Waals density functionals applied to solids. *Phys. Rev. B* **83**, 195131 (2011).